ACS OMEGA

http://pubs.acs.org/journal/acsodf

Article

Organic–Inorganic Hybrid Films of the Sulfate Dawson Polyoxometalate, $[S_2W_{18}O_{62}]^{4-}$, and Polypyrrole for Iodate Electrocatalysis

Amna Yaqub, Mikhail Vagin, James J. Walsh, Fathima Laffir, Indherjith Sakthinathan, Timothy McCormac,* and Mustansara Yaqub

Cite This: *ACS Omega* 2022, 7, 43381–43389

Read Online

ACCESS | Metrics & More | Article Recommendations | Supporting Information

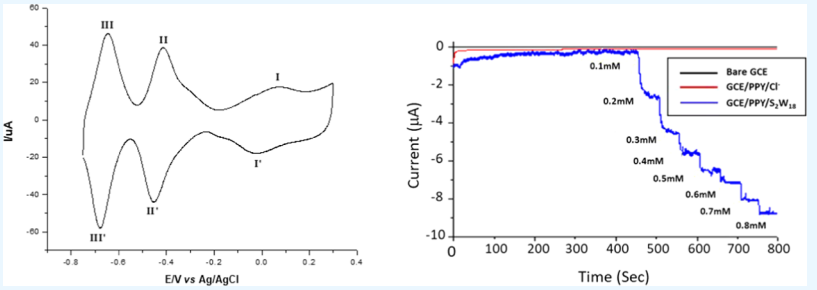

ABSTRACT: The Dawson-type sulfate polyoxometalate (POM) $[S_2W_{18}O_{62}]^{4-}$ has successfully been entrapped in polypyrrole (PPy) films on glassy carbon electrode (GCE) surfaces through pyrrole electropolymerization. Films of varying POM loadings (i.e., thickness) were grown by chronocoulometry. Film-coated electrodes were then characterized using voltammetry, revealing POM surface coverages ranging from 1.9 to 11.7 × 10^{-9} mol·cm^{-2}, and were stable over 100 redox cycles. Typical film morphology and composition were revealed to be porous using atomic force microscopy, scanning electron microscopy, and X-ray photoelectron spectroscopy, and the effects of this porosity on POM redox activity were probed using AC impedance. The hybrid organic–inorganic films exhibited a good electrocatalytic response toward the reduction of iodate with a sensitivity of 0.769 μA·cm^{-2}·μM^{-1}.

INTRODUCTION

The diverse structure and unique electronic properties of polyoxometalates (POMs) make them a promising candidate class for use in electrochemical devices across a broad range of domains including medicine, environmental analysis, energy, and catalysis.[1−6] The most significant property of POMs is their ability to undergo multiple reversible redox processes without significant degradation, rendering them an ideal candidate class for various multielectron catalytic reactions. Importantly, POMs can also be deposited onto various surfaces without significantly altering their characteristic redox properties; immobilization strategies reported to date include the use of sol–gels, self-assembled monolayers, electrodeposition, drop-casting, encapsulation in conducting polymers films, layer-by-layer assembly, and impregnation of support materials.[7−12] Of these approaches, incorporation into a conducting polymer matrix is one of the most promising as it is simple, can be conducted at room temperature, and can be used to carefully control the thickness of immobilized films.[13−16] Another major advantage of using conducting polymers for the fabrication of composites is their known potential use in sensors, corrosion protection coatings, displays, and light-emitting diodes.[16,17]

The Dawson-type polyoxometalates $[M_{18}O_{54}(XO_4)_2]^{n-}$ (where M = Mo, W; X = P, S; n = 4−10) are derived from the M_{12} framework of Keggin-type POMs by removing three MO_6 octahedra and subsequently linking the two M_9 units through corner-sharing. Syntheses of the conventional Dawson-type POMs have been reported previously by several groups by the insertion of two tetrahedral anions into the metal oxide framework such as ClO_4^-, PO_4^{3-}, and SO_4^{2-}.[18−22] The sulfate-based Dawson-type polyoxomolybdate, i.e., α-$[Mo_{18}O_{54}(SO_4)_2]^{4-}$ was synthesized in 1993,[23] while the corresponding tungstate γ*-$[W_{18}O_{54}(SO_4)_2]^{4-}$ was reported in 2001 [20] (described hereafter as $[S_2W_{18}O_{62}]^{4-}$). Both Mo- and W-based sulfate Dawson POMs are extremely stable toward voltammetric cycling and have been used to drive various photo-, electro-, and photoelectrocatalytic reactions.[24−26] Owing to their capacity to go through multiple

Received: March 3, 2022
Accepted: May 12, 2022
Published: November 17, 2022

https://doi.org/10.1021/acsomega.2c01287
ACS Omega 2022, 7, 43381−43389

multielectron redox reactions without undergoing any significant structural changes, POMs have been reported as excellent electrocatalysts for several anions.[27−34] The insertion of POMs into a polymer matrix can improve their catalytic rates toward analytes of interest, including inorganic ions that can act either as intermediates in biochemical reactions or environmental pollutants. A typical example includes the surface anchoring of the iron-substituted Krebs-type POM $[Sb_2W_{20}Fe_2O_{70}(H_2O)_6]^{8-}$ to produce hybrid conducting films using PPy, which showed promising electrocatalytic activity toward the detection of hydrogen peroxide.[33,35] Polypyrrole conducting polymer was used for the immobilization of various transition-metal ion-substituted Dawson-type polyoxometalates (POMs) onto glassy carbon electrodes for the detection of hydrogen peroxide, as reported by Anwar et al.[36] In 2019, Ali et al. prepared a nickel-substituted $Ni_4[(P_8W_{48}O_{184})(WO_2)]^{28-}$, crown-type polyoxometalate doped electrochemically, polymerized with conducting polypyrrole for the electrocatalytic reduction of bromate in water.[37]

Iodine occurs naturally in the environment in various forms, such as iodate and iodide, in different ratios. Low iodine levels can lead to various iodine deficiency disorders (IDDs) including sterility, spontaneous abortion, goiter, and mental retardation.[38] In children, IDDs have been reported to be the main source of preventable brain damage.[39] To achieve the iodine daily requirements of the body, potassium iodate (KIO_3) has been recommended by United Nations Children's Fund (UNICEF) and World Health Organization (WHO) for table salt fortification.[40] However, the release of radioactive isotopes of iodine from nuclear amenities and nonradioactive pollution sources can result in increased environmental concentrations of iodine variants, ultimately leading to bioaccumulation and harmful health effects on animals, such as choriocapillary atrophy and damage to the retina.[41] The primary objective of research in iodine monitoring is thus to fabricate highly sensitive but simple protocols for iodine detection using cost-effective probes that do not require complicated sample preparation or the addition of extra reagents. Various direct and indirect techniques have been established to date for iodate detection including volumetric techniques, ion chromatography, ion-selective membranes,[42] chemiluminescence, solid-phase extraction coupled with spectrophotometry, transient isotachophoresis-capillary zone electrophoresis, fluorescence spectroscopy, and colorimetry.[43] Although these approaches can accurately quantify iodate, they suffer from limitations including complex operating procedures and high cost. Electrochemical methods are preferred for the detection of iodate and periodate by being safer, low-cost, easy to handle, and rapid. As we stated above, polyoxometalates have been used as the best candidates for the modification of electrodes to detect iodate in water. In 2022, Sharifi et al. reported the electrochemical selective detection of iodate using tetra-component nanocomposite consisting of (1,10-(1,4-butanediyl)dipyridinium) ionic liquid, Keggin-type polyoxometalate (POM), and phosphorus-doped electrochemically reduced graphene oxide (P-ERGO) modified glassy carbon electrode.[44] The electrochemistry and redox reaction accompanying the color change and luminescence switching based on Eu^{3+}-containing tungstogermanate polyoxometalate has been used to detect the iodate, bromate, and nitrite.[45] An amperometric sensing platform constructed based on novel attapulgite/polyaniline/phosphomolybdic acid for the determination of iodate was reported by Zhang et al.[46]

Herein, we report the surface immobilization of $[S_2W_{18}O_{62}]^{4-}$ via entrapment in a PPy matrix on glassy carbon electrodes (GCE) for the monitoring of iodate. The organic−inorganic composite films were characterized electrochemically by cyclic voltammetry and AC impedance while surface characterization was performed by applying atomic force microscopy (AFM) and scanning electron microscopy (SEM). Elemental composition was evaluated using X-ray photoelectron spectroscopy (XPS), revealing that the POM was structurally intact within the PPy films. Chronocoulometry was used to control the quantity of electrodeposited POM and cyclic voltammetry (CV) was used to quantify the POM loadings in films of various thicknesses (Γ between 10^9 and 10^8 mol·cm^{-2}). Amperometry was used to monitor the electrocatalytic performance of fabricated films toward the reduction of iodate, with a limit of detection (LOD) of 0.5 μM.

EXPERIMENTAL SECTION

Reagents and Solutions. Pyrrole (Acros Organics, 99%) was purified before use by passing through an activated alumina column to produce a colorless liquid. $[TBA]_4$ γ*-$[S_2W_{18}O_{62}]$ (where TBA = n-tetrabutylammonium) was synthesized as per the literature.[23] Tetrabutylammonium perchlorate ($TBAClO_4$) was recrystallized twice from hot ethanol before use. Alumina powders of three different sizes, i.e., 0.05, 0.3, and 1.0 μm were obtained from CHI Instruments. Ultrapure water from the Milli-Q water purification system was used throughout the experiments. The composition of electrolytes/buffer systems used were (i) 0.1 M Na_2SO_4 with pH range 2.0−3.0, (ii) 0.1 M Na_2SO_4/20 mM CH_3COOH with pH range 3.5−5.0, and (iii) 0.1 M Na_2SO_4/20 mM NaH_2PO_4 having pH 5.5−7.0 (with pH adjusted using 0.1 M H_2SO_4 or 0.1 M NaOH depending on what pH is required).

Instrumentation and Procedures. All of the electrochemical measurements were conducted using a CHI 640 potentiostat and a conventional three-electrode single-compartment electrochemical setup with a disk glassy carbon electrode (GCE) (d = 3 mm, A = 0.0717 cm^2) as the working electrode, Pt wire as the counter electrode, and an Ag/AgCl (3 M KCl) as the reference electrode in aqueous media. For voltammetry in CH_3CN, a Ag/Ag^+ electrode was used (0.01 M $AgNO_3$ + 0.1 M supporting electrolyte in CH_3CN). Prior to each electrochemical investigation, the GCE was cleaned with alumina powder of different grain sizes (i.e., 1.0, 0.3, and finally with 0.05 μm) and rinsed thoroughly with deionized water after each cleaning step. Finally, the electrode was sonicated for 5 minutes and washed with ethanol. All of the redox experiments were carried out at ambient temperature. The working electrolyte/buffer solutions were purged with high-purity nitrogen for 10−15 minutes before each experiment to ensure an oxygen-free environment.

The electrodeposition of $[S_2W_{18}O_{62}]$-doped PPy films on GCE was carried out through chronocoulometry at 0.65 V (charges of 2, 5, and 10 mC)[44] in 0.1 M pyrrole and 0.002 M POM/acetonitrile solution. The coated GCE was washed with ACN to remove the monomer and any weakly bound POM. Electrodeposition was also performed on planar ITO (indium-doped tin oxide) electrodes on glass slides suitable for microscopic analysis.

XPS was performed with a Kratos AXIS 165 spectrometer using monochromatic Al Kα radiation (1486.6 eV). High-resolution scans of specific elements, i.e., C 1s, N 1s, and O 1s,

https://doi.org/10.1021/acsomega.2c01287
ACS Omega 2022, 7, 43381−43389

were recorded at pass energy of 20 eV while pass energy of 100 eV was used for the survey spectrum. The sample surface was saturated with low-energy electrons to neutralize the surface charge. Peak intensities were evaluated by subtracting a Shirley-type background while considering the Scofield factor. Binding energies were calculated using the C 1s peak at the binding energy (BE) of 284.8 eV as a reference.

ITO electrodes coated with POM entrapped in PPy films were used for scanning electron microscopy (SEM) imaging using a Vega 3 LMU Tescan microscope at an accelerating voltage of 3 keV. The low voltage employed ensured that Au sputter coating was not required. AFM analysis was performed using Agilent 5500 in the tapping mode using OTESPA probes (Olympus) with a spring constant of 12−103 N/m and a resonant frequency of 218−342 kHz; PicoView 1.10 was the software used. All of the images were acquired at a resolution of 512 pixels. Software PicoImage Advanced 5.1.1 was used to process the images. Raw topography images were leveled by employing a spatial filter. Height parameters for samples were calculated according to the ISO standard 25178. The area of interest was imaged on the sample with a scan speed of 1 line/second.

RESULTS AND DISCUSSION

Solution Redox Activity of $[S_2W_{18}O_{62}]$. $[TBA]_4[S_2W_{18}O_{62}]$ is insoluble in aqueous media and sparingly soluble in 0.1 M $TBAPF_6/CH_3CN$,[47,48] showing well-defined redox behavior in 0.1 M $TBAClO_4/CH_3CN$. The cyclic voltammogram (Figure 1) reveals six distinguishable

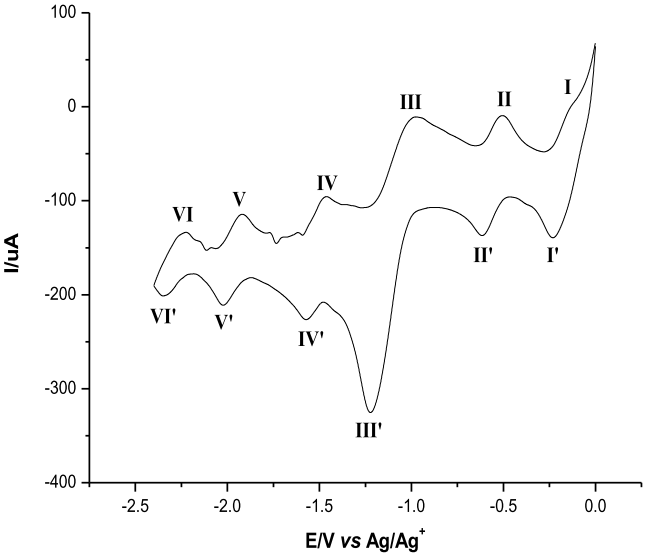

Figure 1. Solution redox behavior of $[S_2W_{18}O_{62}]^{4-}$. The voltammogram was obtained on a glassy carbon working electrode in a 2 mM $[S_2W_{18}O_{62}]^{4-}$ solution in acetonitrile (0.1 M $TBAClO_4$, scan rate 100 mV s^{-1}).

redox couples with half-wave potentials of −0.18, −0.56, −1.1, −1.53, −1.2, and −2.3 V. The peak-to-peak separations of these processes (labeled I/I′ to VI/VI′) were 103, 111, 154, 106, 105, and 102 mV, respectively, which are known to be reversible consecutive single-electron redox processes as described by eqs 1−6.[20,49] Cyclic voltammogram of the bare GC in 0.1 M $TBAClO_4/CH_3CN$ is given in the Supporting Information (Figure S1).

$$[S_2W_{18}O_{62}]^{4-} + 1e^- \leftrightharpoons [S_2W_{18}O_{62}]^{5-} \quad (1)$$

$$[S_2W_{18}O_{62}]^{5-} + 1e^- \leftrightharpoons [S_2W_{18}O_{62}]^{6-} \quad (2)$$

$$[S_2W_{18}O_{62}]^{6-} + 1e^- \leftrightharpoons [S_2W_{18}O_{62}]^{7-} \quad (3)$$

$$[S_2W_{18}O_{62}]^{7-} + 1e^- \leftrightharpoons [S_2W_{18}O_{62}]^{8-} \quad (4)$$

$$[S_2W_{18}O_{62}]^{8-} + 1e^- \leftrightharpoons [S_2W_{18}O_{62}]^{9-} \quad (5)$$

$$[S_2W_{18}O_{62}]^{9-} + 1e^- \leftrightharpoons [S_2W_{18}O_{62}]^{10-} \quad (6)$$

Voltammetry and Impedance of $[S_2W_{18}O_{62}]$-Doped PPy Films. Although $[TBA]_4[S_2W_{18}O_{62}]$ is insoluble in water, after electrodeposition the CVs of the film were recorded in an aqueous electrolyte. The voltammogram of a $[S_2W_{18}O_{62}]$-doped PPy film (Figure 2) revealed the presence of both POM

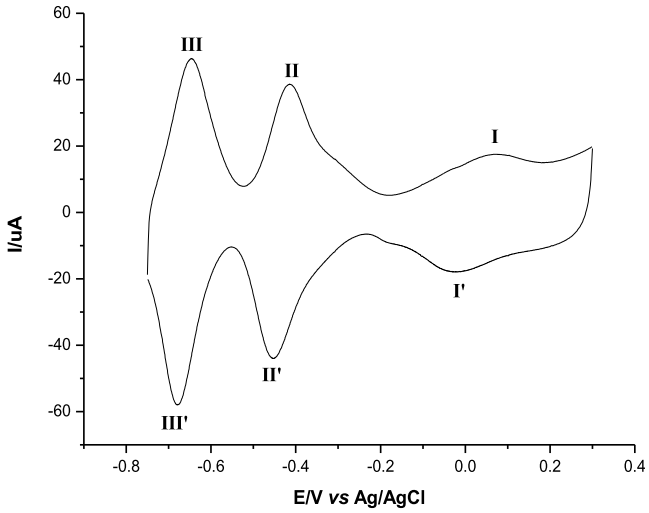

Figure 2. Redox behavior of $[S_2W_{18}O_{62}]^{4-}$-doped polypyrrole film. Cyclic voltammogram was obtained on film-modified glassy carbon working electrode (surface coverage; 1.9 nmol cm^{-2}, electrolyte; 0.1 M Na_2SO_4, pH 2, scan rate; 100 mV s^{-1}).

redox processes and an electrocapacitive current component associated with PPy. The three POM-based redox processes appear well-defined at half-wave potentials of −0.06, −0.43, and −0.66 V (vs Ag/AgCl) with peak-to-peak separations of 90, 43, and 33 mV, respectively, which are slightly greater than the estimated value for an immobilized species. The differences in the voltammetric response of the POM in ACN solution and the PPy film illustrate that changes in the POM environment can result in the stabilization of intermediate redox states; namely, the PPy film and aqueous electrolyte promote the coalescence of POM-based monoelectronic redox couples to merge into apparent two-electron processes, driven by the protonation of the electron-rich species to compensate the accumulated negative charge on the tungsten-oxo framework. This effect resulted in a conversion of six monoelectronic redox processes I−II, III−IV, and V−VI of POM in solution into three two-electron processes I, II, and III, respectively, in a PPy film as described by eqs 7−9. The redox peak I/I′ appears in the conducting region of the polypyrrole backbone, which increases the capacitive current of the I/I′ redox process, while the processes II/II′ and III/III′ are in the polymer's insulating region.[36] A cyclic voltammogram of the PPY/Cl-modified

https://doi.org/10.1021/acsomega.2c01287
ACS Omega 2022, 7, 43381−43389

GCE in 0.1 M $TBAClO_4/CH_3CN$ is given in the Supporting Information (Figure S2).

peak I/II′

$$[S_2W_{18}O_{62}]^{4-} + 2e^- + 2H^+ \leftrightharpoons [H_2S_2W_{18}O_{62}]^{4-} \quad (7)$$

peak II/II′

$$[H_2S_2W_{18}O_{62}]^{4-} + 2e^- + 2H^+ \leftrightharpoons [H_4S_2W_{18}O_{62}]^{4-} \quad (8)$$

peak III/III′

$$[H_4S_2W_{18}O_{62}]^{4-} + 2e^- + 2H^+ \leftrightharpoons [H_6S_2W_{18}O_{62}]^{4-} \quad (9)$$

Upon redox cycling, there is only a slight change of approximately 10−15 mV in both the cathodic and corresponding anodic peak potentials between the initial (E_p^i) and final sweep segments (E_p^f) for the film shown in Figure S3. Scan rate studies of $[S_2W_{18}O_{62}]$/PPy on GCE revealed a linear relationship between peak current and scan rate, indicative of the surface-confined behavior (Figure S4a). By tuning the charge passed during electrodeposition, films of varying thicknesses were grown, with thicker films showing increased peak-to-peak separation, suggesting a hindered charge transfer through these thicker films (Table S1). This phenomenon was [km k] manifested by the change in the rate-determining step of POM redox processes (Figure S4) from surface-confined to diffusion-controlled moderate scan rates (100 $mV{\cdot}s^{-1}$) for thick $[S_2W_{18}O_{62}]$/PPy films. The values of FWHM, i.e., full width at half-maximum of oxidation peaks for redox processes on $[S_2W_{18}O_{62}]$-doped PPy films were 62, 92, and 96 mV for I/I′, II/II′, and III/III′ redox processes, respectively, which seem to be larger than the expected value of 45.3 mV for a surface-confined bielectronic process. This effect is typical for POM-doped films and is attributed to electrostatic repulsion between the highly charged immobilized POM units.[15] The stability of POM-PPy films toward redox cycling in aqueous electrolyte (100 cycles) showed ca. 93% peak current retention for II and III redox processes. The thicker film shows decreased stability, likely due to the reduced ionic diffusion rates through the thicker films.

The pH study of the voltammetric response of $[S_2W_{18}O_{62}]$/PPy on GCE showed a considerable influence of pH on redox processes II and III, while process I revealed a minor pH dependence (Figure 3). The Nernstian shifts (61 mV/pH unit) of the half-wave potentials observed for processes II and III illustrate the involvement of equal numbers of protons and electrons.

The properties of polymerized membranes were investigated by electrochemical impedance spectroscopy (EIS) in an aqueous electrolyte. The obtained spectra are typical for porous electric double-layer electrodes[50] (Figure 4) utilized in electrocapacitive energy storage technologies. Here, the capacitive behavior is maintained by the pseudocapacitive potential of PPy. The data at high frequencies (point A) are dominated by serial ohmic resistances from the electrode and the electrolyte. The difference in the projections of points A and B represents the diffuse layer resistance, R_D. The data between points A and B represent the ionic diffusion due to charge compensation within the polymer (i.e., a charging process). The diffusion-controlled data region can be linearized in a Z′ vs Z″ plot, where Z′ and Z″ are the real and imaginary components of the impedance, respectively, with a slope equal to the ratio between the time constants of ion diffusion within the film and in the bulk electrolyte. Finally, the low-frequency range (between points B and C) is dominated by the film capacitance. The data located over the linear portion of this

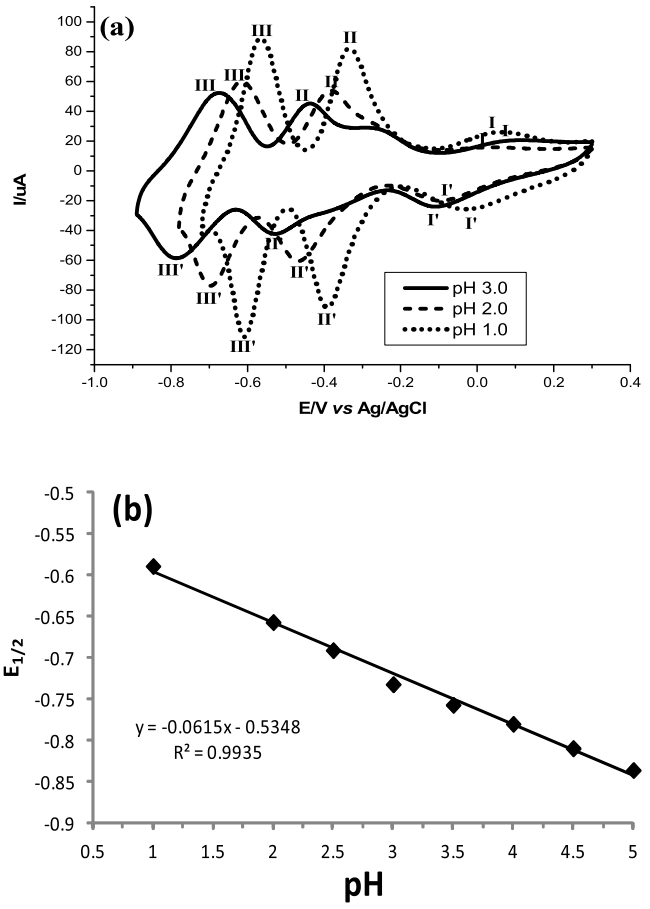

Figure 3. (a) Cyclic voltammograms of $[S_2W_{18}O_{62}]$/PPy composite film (surface coverage 4.36×10^{-9} mol cm^{-2} at pH 1.0, 2.0, and 3.0. Scan rate 100 mV s^{-1}). (b) Graph between $E_{1/2}$ and pH for the second W−O redox couple of $[S_2W_{18}O_{62}]$ anion.

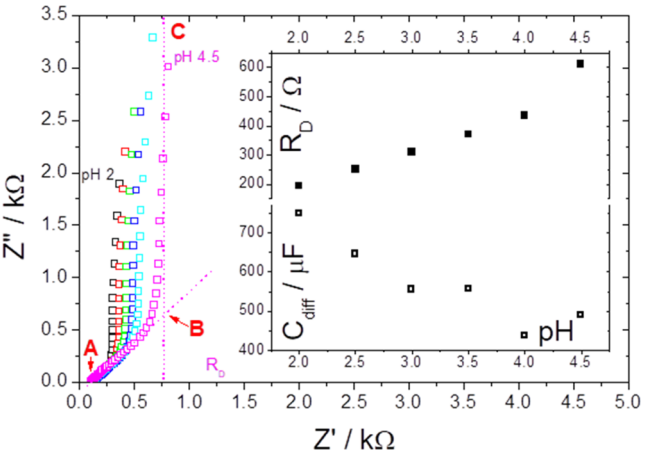

Figure 4. Enhancement of ionic diffusion by proton doping. The spectra of $[S_2W_{18}O_{62}]$/PPy film-modified GCE in Nyquist coordinates were acquired in the background electrolyte (0.1 M Na_2SO_4; −0.39 V bias) of different pH values. Insets: pH dependencies of diffuse layer resistance and differential capacitance of the films.

https://doi.org/10.1021/acsomega.2c01287
ACS Omega 2022, 7, 43381−43389

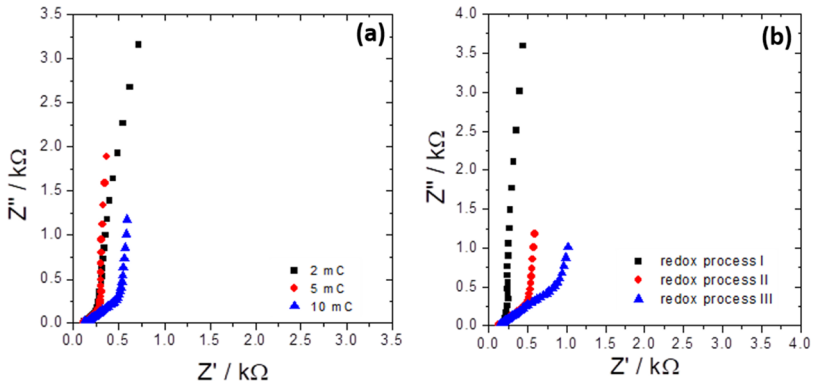

Figure 5. (a) Thickness dependence of electrocapacitive properties. The spectra of $[S_2W_{18}O_{62}]$/PPy film-modified GCE in Nyquist coordinates were acquired after polymerization at different integral charges. (b) Impedance spectra in Nyquist coordinates were obtained at the potentials of POM redox processes (−0.01, −0.39, and −0.67 V, for processes I, II, and III, respectively; 5 mC film).

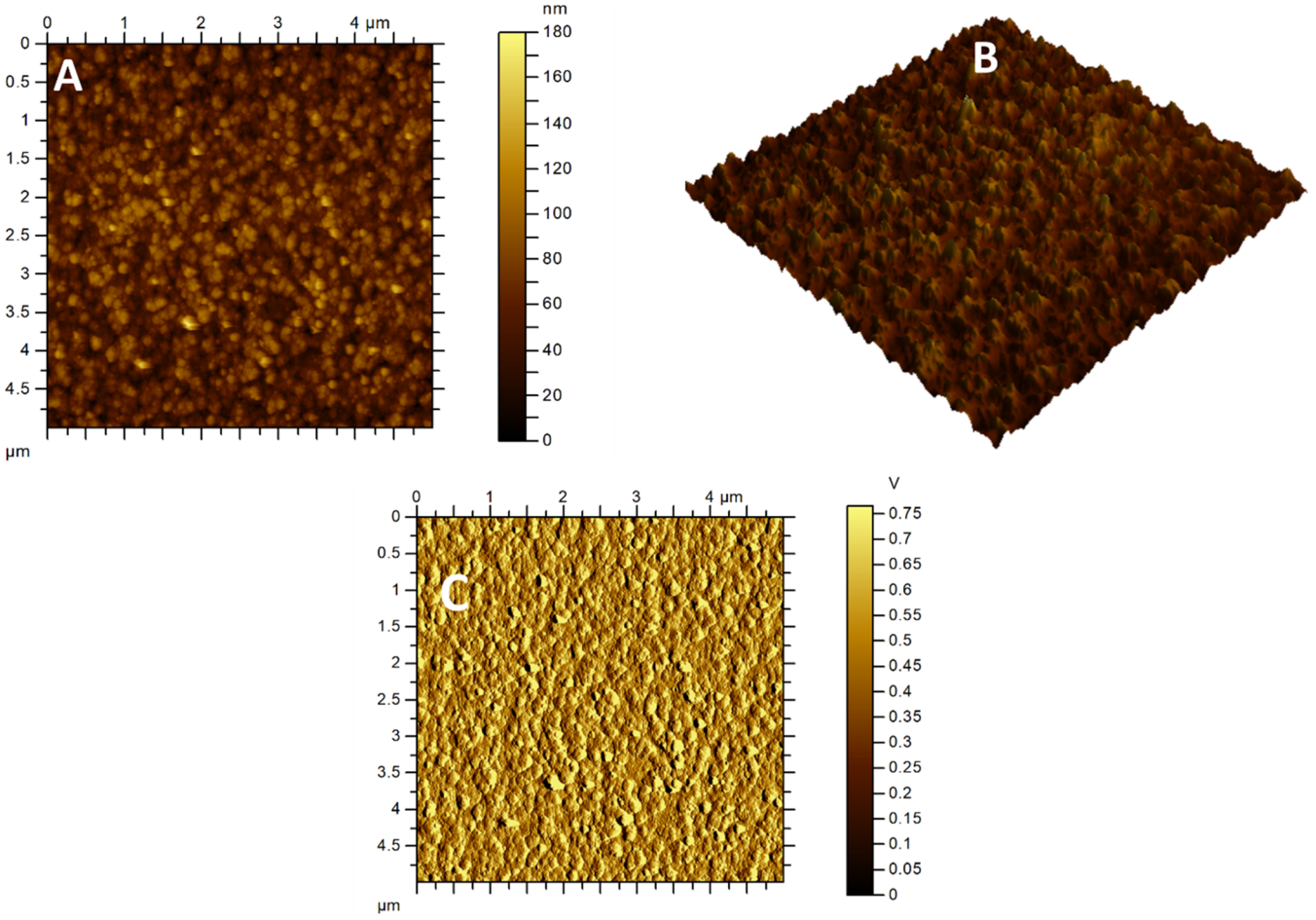

Figure 6. AFM images of the S_2W_{18}/PPy film grown on the ITO slide. (A) and (B) 2D and 3D topography images of the film, while (C) is the amplitude image of the film.

low-frequency region can be linearized in a Z″ vs $(1/f)$ plot, where f is frequency, yielding a slope equal to $(2\pi C_{diff})^{-1}$, where C_{diff} is the differential capacitance. The analysis of the data was carried out without equivalent circuit fitting to avoid model-dependent interpretation.

The decrease of pH from 4.5 to 2 led to the shrinkage of the diffusion control region of frequencies of spectra recorded at the POM redox process II (Figure 4) due to the doping of PPy by protons. This was represented by the threefold decrease in R_D and increase in C_{diff} of the films (insets of Figure 4). This may be due to increased rates of ionic diffusion (ionic conductivity) and the sum differences of accommodated charges, respectively. The ratio between time constants of inner and outer ionic processes showed pH-independent values close to 1, illustrating that they have similar contributions.

The increase in film thickness achieved by passing more charge during electropolymerization leads to an expansion of the diffusion-controlled frequency region (Figure 5). This is rationalized as a general increase in the diffuse layer resistance due to restricted ion diffusion into deeper pores during the

https://doi.org/10.1021/acsomega.2c01287
ACS Omega 2022, 7, 43381−43389

charging process. The C_{diff} scales with film thickness, with a 5 mC polymerization charge, passed yielding a film with increased capacitance. This illustrates the porosity of the PPy film, with the bulk of the film permitting facile ion diffusion. The increase in polymerization charge led to a slight decrease in the time constants ratio for inner and outer processes, which might illustrate the formation of large pores during longer polymerization times due to agglomeration.

The characteristics of other POM-based redox processes (I and III) was explored (Figure 5b). The measurements at the potentials of processes I, II, and III showed increased diffusion layer resistance with increased negative polarization, probably due to a lack of PPy conductivity by dedoping at negative potentials. Process II exhibited a 4× larger C_{diff} with respect to process I, which potentially illustrated a change from a charge storage mechanism from pseudocapacitive PPy-associated process I to an intercalative process I, where the contribution from PPy was smaller. The decrease in the time constants ratio for inner and outer ionic processes was observed with negative polarization, which could be a result of the transition from PPy-dominated to POM-dominated ionic phenomenon.

Spectroscopic and Microscopic Characterizations of $[S_2W_{18}O_{62}]$-Doped PPy Films. The surface features and homogeneity of films deposited on planar ITO electrodes were explored using SEM (Figure S5). The $[S_2W_{18}O_{62}]$/PPy film-modified surface appeared to be fully covered with an array of tiny bead-like domains of varying sizes. Higher magnification of the micrographs revealed that the darker parts were also covered with closely spaced irregular-shaped spheres of micrometer to submicrometer dimensions. The voltammetric cycling did not produce significant alteration in the surface morphology of the immobilized film. A small fusion of the deposited particles can be seen after cycling. Figure 6 shows the AFM 2D and 3D topography image of $[S_2W_{18}O_{62}]$/PPy electrodeposited on ITO. Hemispherically shaped globular structures of varying diameters could be seen all over the imaged area. Root mean square surface roughness was evaluated as 19.6 nm. Some phase contrast was observed, suggesting a homogeneous nature of the polymer film within the examined area.

A film of $[S_2W_{18}O_{62}]$/PPy on ITO was also investigated by XPS with the elemental percentage composition being provided in Table 1. Figure S6 presents the high-resolution

Table 1. Elemental Composition and Chemical State of Elements Evaluated by XPS Analysis

	N		W	S	O
element	C-N	C−N+	W (+6)	S−O	oxide
BE (eV)	400.3	401.8	36.3	170.1	531.2
atomic %	**8.1**		**6.7**	**1.2**	**31.6**
	5.3	*2.8*	*6.7*	*1.2*	*31.6*

spectra of the elements, i.e., W 4f, S 2p, C 1s, and N 1s. W is detected as a doublet for $4f_{7/2}$ with a BE of 36.3 eV, typical for W^{6+} as shown in Figure S6a. S appears as a $2p_{3/2}$ doublet at 170.1 eV, indicative of S−O bonding (Figure S6b). The N 1s spectrum (Figure S6c) is deconvoluted into two peaks with the lower BE peak at *ca.* 400.3 eV assigned to the neutral N and the other peak at 401.8 eV assigned to N^+ in PPy. The satellite peak at 291.5 eV is indicative of the unsaturated C=C bonding in PPy. The doping level of the hybrid film can be assessed from the N^+/N ratio, which is 0.53 in this study.

Electrocatalytic Properties of $[S_2W_{18}O_{62}]$-doped PPy Films. The additions of iodate as a model substance for the electrocatalytic evaluation of $[S_2W_{18}O_{62}]$/PPy films on GCE in an aqueous electrolyte at pH 4.5 led to a rise in cathodic peak currents at the third redox couple of immobilized POM (Figure 7a) with a subsequent decrease in corresponding

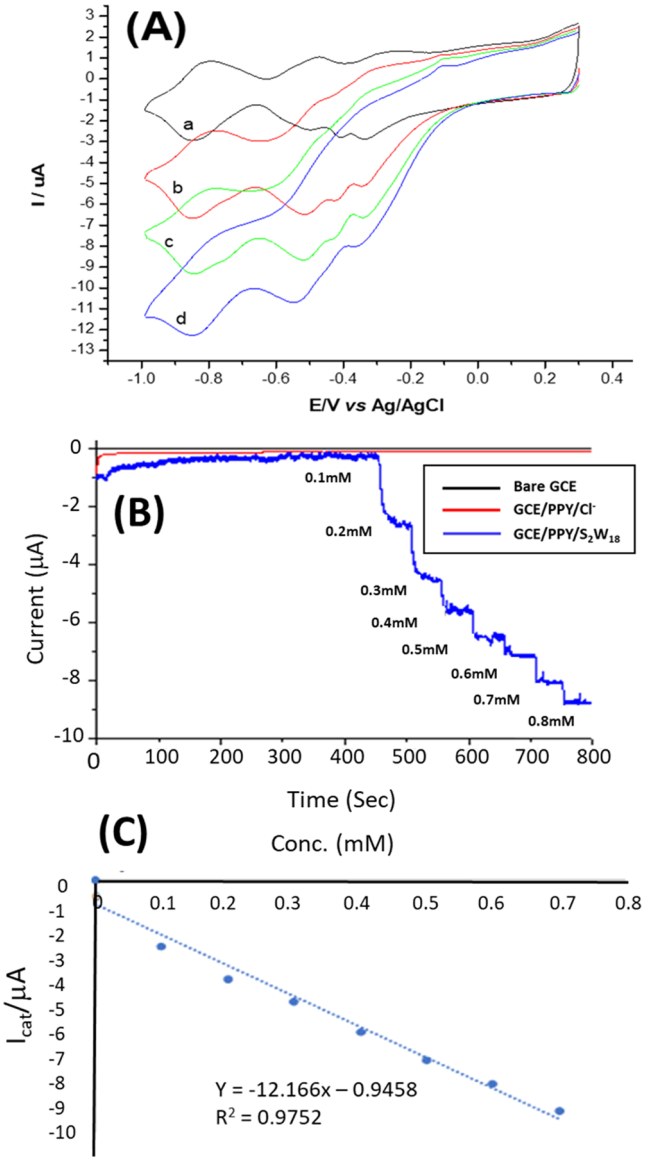

Figure 7. (A) Cyclic voltammetry of the $[S_2W_{18}O_{62}]$/PPy film (surface coverage 2.38 × 10^{-9} mol cm^{-2}) at different concentrations (mM), i.e., (a) 0.0, (b) 0.4, (c) 0.8, and (d) 1.0 $NaIO_3$ in buffer pH 4.5. Scan rate is 0.005 Vs^{-1}. (B) Amperograms of blank (black), PPy (red), and $[S_2W_{18}O_{62}]$/PPy (purple) coated electrodes on sequential additions of 0.1 mM iodate (E; −0.83 V; pH 4.5). (C) Calibration plot between I_{cat} and concentration of iodate.

anodic peak current. It can also be supported by the fact that the reduction reaction of iodate requires the presence of 6 electrons and 6 equiv of protons (See eqs 7−9 and 10). The reaction scheme is

$$IO_3^- + 6e^- + 6H^+ \leftrightharpoons I^- + 3H_2O \quad (10)$$

A linear relationship of the cathodic peak current of process III with the iodate concentration represents the analytical

https://doi.org/10.1021/acsomega.2c01287
ACS Omega 2022, 7, 43381−43389

Table 2. Some Literature on Iodate Sensors, Techniques Used, and Their Parameters

sr., no	active material	technique	limit of detection (LOD) (μM)	linear range (μM)	sensitivity (μA μM^{-1} cm^{-2})	refs
1	MCNF (mechanically treated pyrolytic carbon nanofiber)	voltammetry	0.59 and 1.41	5−700		54
2	ZnO nanotubes assembled on the Au-coated glass substrates	potentiometry, potentiometric titration	0.5	1−100[a]		55
3	zeolite-modified carbon paste	voltammetry	0.64	4−100		56
4	phosphomolybdate/polybezidine/Ag np	amperometry	1.45		0.00057	57
5	MWCNTs/Prussian blue/Pt	cyclic voltammetry	8.30	34.0−268.3	0.021	58
6	GCE/MWCNTs/$[C_8Py]$ $[PF_6]$-PMo_{12}	amperometry	15	0.02−2[a]	0.19	59
7	C cloth/PANI/WO_3	amperometry	2.7	10−500	0.68	60
8	S_2W_{18}/polypyrrole	amperometry	0.5	100−700	0.769	this work

[a]mM.

performance of the electrocatalytic film, with a linear region between a range of 100 μM and 0.7 mM. As previously stated, Dawson-type POMs are stable over a wide pH range and the pH of the contacting electrolyte influences their electrochemical behavior.[51] Figure 7a shows a small additional peak, which is due to the splitting of the bielectronic peak into two monoelectronic peaks in the pH 4.5 buffer.

Amperometric detection of iodate was performed in pH 4.5 buffer at a potential of −0.83 V (vs Ag/AgCl), corresponding to the $E_{1/2}$ for immobilized process III (Figure 2). Figure 7b shows the amperograms of a bare GCE electrode (black), GCE/PPy only (red), and GCE/$[S_2W_{18}O_{62}]$/PPy with a surface coverage of 1.88 mol cm^{-2} (blue) upon successive additions of iodate. The films were stabilized for a specific time before the addition of the analyte. Figure 7 shows that $[S_2W_{18}O_{62}]$/PPy displays a promising electrocatalytic response to the reduction of iodate, with no comparable activity for the bare GCE electrode and the PPy film alone. The calibration curve based on the amperometric data obtained from three equivalently prepared $[S_2W_{18}O_{62}]$/PPy films with similar surface coverages were obtained (Figure 7c), revealing sensitivity of 0.569 $\mu A \cdot \mu M^{-1} \cdot cm^{-2}$ with a linear range of 100 μM−0.7 mM. The limit of detection (LOD) was calculated to be 0.5 μM based on n = 3 measurements, which were comparable to many of the previously reported detection systems for iodate (Table 2). Similar observations were reported in the previous literature.[52,53] The repeatability of the $[S_2W_{18}O_{62}]$/PPy composite film for the detection of iodate was also determined through three amperometric detections of iodate, and an RSD value was found to be 3.5%.

From the cyclic voltammetric responses, it is noted that the addition of 100 μM iodate ion concentration raises the reduction peak current to around 0.34 V in the first reduction region (I/I′) and reaches a maximum of around −0.83 V in the third reduction region (III/III′). This indicates that the electrocatalytic reduction of iodate is caused by the six-electron product of $[S_2W_{18}O_{62}]$/PPy as mentioned in eq 10.

CONCLUSIONS

The organic−inorganic hybrid films based on PPy- and sulfate-containing POM entrapped as a counterion were fabricated via electrochemical polymerization. The developed films were characterized by electrochemical and physical methods showing the change in the rate-determining step of the electrode process with increased film thickness. The films revealed considerable stability upon voltammetric cycling combined with electrocatalytic functionality toward iodate reduction at pH 4.5 and comparable LOD and linear range with a range of other electrocatalytic devices for iodate detection. Given the extraordinary ability of POMs to accept/donate multiple electrons, future work will focus on extending this sensor technology to other multielectron reduction processes, for example, N_2 reduction to NH_3.

ASSOCIATED CONTENT

Supporting Information

The Supporting Information is available free of charge at https://pubs.acs.org/doi/10.1021/acsomega.2c01287.

Electrochemical and impedance spectroscopy data for the films of different surface thicknesses are included in the supporting information. It also includes images from scanning electron microscopy (PDF)

AUTHOR INFORMATION

Corresponding Author

Timothy McCormac − *Electrochemistry Research Group, Department of Applied Science, Dundalk Institute of Technology, Dundalk A91 K584 County Louth, Ireland;* orcid.org/0000-0002-9096-1248; Email: Tim.mccormac@dkit.ie

Authors

Amna Yaqub − *University of Engineering and Technology, Lahore, Punjab 39161, Pakistan;* orcid.org/0000-0001-8381-0620

Mikhail Vagin − *Laboratory of Organic Electronics, Department of Science and Technology, Linköping University, SE-601 74 Norrköping, Sweden;* orcid.org/0000-0001-8478-4663

James J. Walsh − *School of Chemical Sciences, Dublin City University, Dublin 9, Ireland; National Centre for Sensor Research, Dublin City University, Dublin 9, Ireland;* orcid.org/0000-0003-4862-8449

Fathima Laffir − *Materials and Surface Science Institute, University of Limerick, Limerick V94 T9PX, Ireland*

Indherjith Sakthinathan − *Electrochemistry Research Group, Department of Applied Science, Dundalk Institute of Technology, Dundalk A91 K584 County Louth, Ireland;* orcid.org/0000-0001-5623-084X

Mustansara Yaqub − *Interdisciplinary Research Centre in Biomedical Materials (IRCBM), COMSATS University Islamabad, Lahore, Punjab 54000, Pakistan*

Complete contact information is available at:

https://doi.org/10.1021/acsomega.2c01287
ACS Omega 2022, 7, 43381−43389

https://pubs.acs.org/10.1021/acsomega.2c01287

Funding

Funding from Dundalk Institute of Technology was used to support the research.

Notes

The authors declare no competing financial interest.

■ ACKNOWLEDGMENTS

The authors acknowledge the Dundalk Institute of Technology for funding this project, MSSI, Bernal Institute, Limerick, for the surface analysis support.

■ REFERENCES

(1) Yang, B.; Pignatello, J. J.; Qu, D.; Xing, B. Reoxidation of photoreduced polyoxotungstate ($[PW_{12}O_{40}]^{4-}$) by different oxidants in the presence of a model pollutant. Kinetics and reaction mechanism. *J. Phys. Chem. A* **2015**, *119*, 1055−1065.

(2) Haviv, E.; Shimon, L. J.; Neumann, R. Photochemical reduction of CO_2 with visible light using a polyoxometalate as photoreductant. *Chem. Eur. J* **2017**, *23*, 92−95.

(3) Wang, H.; Hamanaka, S.; Nishimoto, Y.; Irle, S.; Yokoyama, T.; Yoshikawa, H.; Awaga, K. In operando X-ray absorption fine structure studies of polyoxometalate molecular cluster batteries: polyoxometalates as electron sponges. *J. Am. Chem. Soc.* **2012**, *134*, 4918−4924.

(4) Li, F.; Carpenter, S. H.; Higgins, R. F.; Hitt, M. G.; Brennessel, W. W.; Ferrier, M. G.; Cary, S. K.; Lezama-Pacheco, J. S.; Wright, J. T.; Stein, B. W.; et al. Polyoxovanadate−alkoxide clusters as a redox reservoir for iron. *Inorg. Chem.* **2017**, *56*, 7065−7080.

(5) Chen, W.-H.; Mi, J.-X. A new redox-based approach for synthesizing a mixed-valence hybrid polymolybdate uncommonly bicapped by Cr (III) coordination complexes. *Polyhedron* **2015**, *85*, 117−123.

(6) Dong, B.-X.; Wu, Y.-C.; Tian, H.; Liu, C.-B.; Liu, W.-L.; Teng, Y.-L. Synthesis, Crystal Structure and Electrochemical Properties of A New 2D Network Containing Linear $\{\varepsilon\text{-}H_2PMo_8V^{VI}Mo_4O_{40}Zn_4\}^{\infty}$ Inorganic Chain. *J. Clust. Sci.* **2016**, *27*, 361−371.

(7) Miras, H. N.; Vilà-Nadal, L.; Cronin, L. Polyoxometalate based open-frameworks (POM-OFs). *Chem. Soc. Rev.* **2014**, *43*, 5679−5699.

(8) Zhao, J.-W.; Li, Y.-Z.; Chen, L.-J.; Yang, G.-Y. Research progress on polyoxometalate-based transition-metal−rare-earth heterometallic derived materials: synthetic strategies, structural overview and functional applications. *Chem. Commun.* **2016**, *52*, 4418−4445.

(9) Okuhara, T.; Mizuno, N.; Misono, M.Catalytic chemistry of heteropoly compounds. In *Adv. Catal.*, Elsevier: 1996; *41*, pp 113−252.

(10) Walsh, J. J.; Bond, A. M.; Forster, R. J.; Keyes, T. E. Hybrid polyoxometalate materials for photo (electro-) chemical applications. *Coord. Chem. Rev.* **2016**, *306*, 217−234.

(11) Yaqub, M.; Walsh, J. J.; Keyes, T. E.; Proust, A.; Rinfray, C.; Izzet, G.; McCormac, T.; Forster, R. J. Electron transfer to covalently immobilized Keggin polyoxotungstates on gold. *Langmuir* **2014**, *30*, 4509−4516.

(12) Imar, S.; Yaqub, M.; Maccato, C.; Dickinson, C.; Laffir, F.; Vagin, M.; McCormac, T. Nitrate and Nitrite Electrocatalytic Reduction at Layer-by-Layer Films Composed of Dawson-type Heteropolyanions Mono-substituted with Transitional Metal Ions and Silver Nanoparticles. *Electrochim. Acta* **2015**, *184*, 323−330.

(13) Zhang, H.-Y.; Miao, A.-J.; Jiang, M. Fabrication, characterization and electrochemistry of organic−inorganic multilayer films containing polyoxometalate and polyviologen via layer-by-layer self-assembly. *Mater. Chem. Phys.* **2013**, *141*, 482−487.

(14) Liu, R.; Li, S.; Yu, X.; Zhang, G.; Zhang, S.; Yao, J.; Zhi, L. A general green strategy for fabricating metal nanoparticles/polyoxometalate/graphene tri-component nanohybrids: enhanced electrocatalytic properties. *J. Mater. Chem.* **2012**, *22*, 3319−3322.

(15) Yaqub, M.; Walsh, J.; Laffir, F.; Olstoorn, P.; Kailas, L.; Forster, R.; Keyes, T. E.; Vagin, M.; McCormac, T. Polypyrrole entrapped 18-molybdodisulphate anion for the detection of hydrogen peroxide. *Electrochim. Acta* **2018**, *287*, 78−86.

(16) Gomez-Romero, P. Hybrid organic−inorganic materials—in search of synergic activity. *Adv. Mater.* **2001**, *13*, 163−174.

(17) Shimidzu, T.; Ohtani, A.; Aiba, M.; Honda, K. Electrochromism of a conducting polypyrrole−phosphotungstate composite electrode. *J. Chem. Soc., Faraday Trans. 1* **1988**, *84*, 3941−3949.

(18) Hölscher, M.; Englert, U.; Zibrowius, B.; Hölderich, W. F. $(H_3N(CH_2)_6NH_3)_4$ $[W_{18}P_2O_{62}]\cdot 3H_2O$, ein mikroporöser Festkörper aus Dawson-Anionen und Hexamethylendiamin. *Angew. Chem.* **1994**, *106*, 2552−2554.

(19) Zhang, J.; Bond, A. M.; Richardt, P. J.; Wedd, A. G. Voltammetric Reduction of α-and γ*-$[S_2W_{18}O_{62}]^{4-}$ and α-, β-, and γ-$[SiW_{12}O_{40}]^{4-}$: Isomeric Dependence of Reversible Potentials of Polyoxometalate Anions Using Data Obtained by Novel Dissolution and Conventional Solution-Phase Processes. *Inorg. Chem.* **2004**, *43*, 8263−8271.

(20) Richardt, P. J. S.; Gable, R. W.; Bond, A. M.; Wedd, A. G. Synthesis and Redox Characterization of the Polyoxo Anion, γ*-$[S_2W_{18}O_{62}]^{4-}$: A Unique Fast Oxidation Pathway Determines the Characteristic Reversible Electrochemical Behavior of Polyoxometalate Anions in Acidic Media. *Inorg. Chem.* **2001**, *40*, 703−709.

(21) Way, D. M.; Cooper, J. B.; Sadek, M.; Vu, T.; Mahon, P. J.; Bond, A. M.; Brownlee, R. T.; Wedd, A. G. Systematic Electrochemical Synthesis of Reduced Forms of the α-$[S_2Mo_{18}O_{62}]^{4-}$Anion1. *Inorg. Chem.* **1997**, *36*, 4227−4233.

(22) Neier, R.; Trojanowski, C.; Mattes, R. Reduced polyoxomolybdates with the Keggin and Dawson structures: preparation and crystal structures of two-electron reduced $[K\ (18\text{-crown}^{-6})]_2[N(PPh_3)_2]_2$ $[HPMo_{12}O_{40}]\cdot$ 8MeCN· 18-crown-6 and four-electron reduced $[NBu_{n4}]_5[H_3S_2Mo_{18}O_{62}]\cdot$4MeCn (18-crown-6= 1, 4, 7, 10, 13, 16-hexaoxacyclooctadecane). *J. Chem. Soc., Dalton Trans.* **1995**, 2521−2528.

(23) Cooper, J. B.; Way, D. M.; Bond, A. M.; Wedd, A. G. A green heteropoly blue: isolation of a stable, odd oxidation level in a Dawson molybdate anion,$[S_2Mo_{18}O_{62}]^5$. *Inorg. Chem.* **1993**, *32*, 2416−2420.

(24) Walsh, J. J.; Zhu, J.; Zeng, Q.; Forster, R. J.; Keyes, T. E. Self assembled composites of luminescent Ru (ii) metallopolymers and the Dawson polyoxometalate α-$[Mo_{18}O_{54}(SO_4)_2]^{4-}$. *Dalton Trans.* **2012**, *41*, 9928−9937.

(25) Fay, N.; Dempsey, E.; McCormac, T. Assembly, electrochemical characterisation and electrocatalytic ability of multilayer films based on $[Fe(bpy)_3]^{2+}$, and the Dawson heteropolyanion, $[P_2W_{18}O_{62}]^{6-}$. *J. Electroanal. Chem.* **2005**, *574*, 359−366.

(26) Bernardini, G.; Wedd, A. G.; Zhao, C.; Bond, A. M. Photochemical oxidation of water and reduction of polyoxometalate anions at interfaces of water with ionic liquids or diethylether. *Proc. Natl. Acad. Sci. U.S.A.* **2012**, *109*, 11552−11557.

(27) Cao, G.; Xiong, J.; Xue, Q.; Min, S.; Hu, H.; Xue, G. Organic−inorganic heteropoly blue based on Dawson-type molybdosulfate and organic dye and its characterization and application in electrocatalysis. *Electrochim. Acta* **2013**, *106*, 465−471.

(28) Yaqub, M.; Imar, S.; Laffir, F.; Armstrong, G.; McCormac, T. Investigations into the electrochemical, surface, and electrocatalytic properties of the surface-immobilized polyoxometalate, TBA_3K-$[SiW_{10}O_{36}(PhPO)_2]$. *ACS Appl. Mater. Interfaces* **2015**, *7*, 1046−1056.

(29) Lv, H.; Geletii, Y. V.; Zhao, C.; Vickers, J. W.; Zhu, G.; Luo, Z.; Song, J.; Lian, T.; Musaev, D. G.; Hill, C. L. Polyoxometalate water oxidation catalysts and the production of green fuel. *Chem. Soc. Rev.* **2012**, *41*, 7572−7589.

(30) Ammam, M. Polyoxometalates: formation, structures, principal properties, main deposition methods and application in sensing. *J. Mater. Chem. A* **2013**, *1*, 6291−6312.

(31) Lu, X.-F.; Liao, P.-Q.; Wang, J.-W.; Wu, J.-X.; Chen, X.-W.; He, C.-T.; Zhang, J.-P.; Li, G.-R.; Chen, X.-M. An alkaline-stable, metal

hydroxide mimicking metal−organic framework for efficient electrocatalytic oxygen evolution. *J. Am. Chem. Soc* **2016**, *138*, 8336−8339.
(32) Papagianni, G. G.; Stergiou, D. V.; Armatas, G. S.; Kanatzidis, M. G.; Prodromidis, M. I. Synthesis, characterization and performance of polyaniline−polyoxometalates (XM12, X= P, Si and M= Mo, W) composites as electrocatalysts of bromates. *Sens. Actuators, B* **2012**, *173*, 346−353.
(33) Ernst, A. Z.; Sun, L.; Wiaderek, K.; Kolary, A.; Zoladek, S.; Kulesza, P. J.; Cox, J. A. Synthesis of Polyoxometalate-Protected Gold Nanoparticles by a Ligand-Exchange Method: Application to the Electrocatalytic Reduction of Bromate. *Electroanalysis* **2007**, *19*, 2103−2109.
(34) Medetalibeyoğlu, H.; Manap, S.; Yokuş, ÖA.; Beytur, M.; Kardaş, F.; Akyıldırım, O.; Özkan, V.; Yüksek, H.; Yola, M. L.; Atar, N. Fabrication of Pt/Pd nanoparticles/polyoxometalate/ionic liquid nanohybrid for electrocatalytic oxidation of methanol. *J. Electrochem. Soc.* **2018**, *165*, F338.
(35) Foster, K.; Bi, L.; McCormac, T. Immobilisation of the polyoxometallate cluster, $K_6NaH\,[Sb_2W_{20}Fe_2O_{70}(H_2O)_6]\cdot 29H_2O$, in a polypyrrole film. *Electrochim. Acta* **2008**, *54*, 868−875.
(36) Anwar, N.; Vagin, M.; Laffir, F.; Armstrong, G.; Dickinson, C.; McCormac, T. Transition metal ion-substituted polyoxometalates entrapped in polypyrrole as an electrochemical sensor for hydrogen peroxide. *Analyst* **2012**, *137*, 624−630.
(37) Ali, B.; Laffir, F.; Kailas, L.; Armstrong, G.; Kailas, L.; O'Connell, R.; O'Connell, R.; McCormac, T. Electrochemical Characterisation of NiII-Crown-Type Polyoxometalate-Doped Polypyrrole Films for the Catalytic Reduction of Bromate in Water. *Eur. J. Inorg. Chem.* **2019**, *2019*, 394−401.
(38) Zimmermann, M. B.; Jooste, P. L.; Pandav, C. S. Iodine-deficiency disorders. *The Lancet* **2008**, *372*, 1251−1262.
(39) Yadav, K.; Pandav, C. S. National iodine deficiency disorders control programme: current status & future strategy. *Indian J. Med. Res.* **2018**, *148*, 503.
(40) Wang, T.; Zhao, S.; Shen, C.; Tang, J.; Wang, D. Determination of iodate in table salt by transient isotachophoresis−capillary zone electrophoresis. *Food Chem.* **2009**, *112*, 215−220.
(41) Niazi, A. K.; Niazi, S. K. Endocrine effects of Fukushima: Radiation-induced endocrinopathy. *Indian J. Endocrinol. Metab.* **2011**, *15*, 91.
(42) Chandra, S.; Lokesh, K. S.; Langa, H. Iodide recognition by the N,N-bis-succinamide-based dendritic molecule $[CH_2C(O)NHC(CH_2CH_2C(O)OtBu)_3]_2$. *Sens. Actuators, B* **2009**, *137*, 350−356.
(43) Fardousi, M.*Determination of Iodine Content in Different Brands Table Salt of Bangladesh*; East West University, 2012.
(44) Sharifi, M.; Dianat, S.; Hosseinian, A. Electrochemical investigation and amperometry determination iodate based on ionic liquid/ polyoxotungstate/P-doped electrochemically reduced graphene oxide multi-component nanocomposite modified glassy carbon electrode. *RSC Adv.* **2021**, *11*, 8993−9007.
(45) Wang, B.; Meng, R-Q.; Xu, L-X.; Wu, L-X.; Bi, L-H. A novel detection of nitrite, iodate and bromate based on a luminescent polyoxometalate. *Anal. Methods* **2013**, *5*, 885−890.
(46) Zhang, S.; He, P.; Lei, W.; Zhang, G. Novel attapulgite/polyaniline/phosphomolybdic acid-based modified electrode for the electrochemical determination of iodate. *J. Electroanal. Chem.* **2014**, *724*, 29−35.
(47) McCormac, T.; Farrell, D.; Drennan, D.; Bidan, G. Immobilization of a series of Dawson type heteropolyanions. *Electroanalysis* **2001**, *13*, 836−842.
(48) Baffert, C.; Boas, J. F.; Bond, A. M.; Kögerler, P.; Long, D. L.; Pilbrow, J. R.; Cronin, L. Experimental and Theoretical Investigations of the Sulfite-Based Polyoxometalate Cluster Redox Series: α-and β-$[Mo_{18}O_{54}(SO_3)_2]^{4-/5-/6-}$. *Chem. Eur. J* **2006**, *12*, 8472−8483.
(49) Fay, N.; Bond, A. M.; Baffert, C.; Boas, J. F.; Pilbrow, J. R.; Long, D.-L.; Cronin, L. Structural, electrochemical, and spectroscopic characterization of a redox pair of sulfite-based polyoxotungstates: α-$[W_{18}O_{54}(SO_3)_2]^{4-}$and α-$[W_{18}O_{54}(SO3)\ 2]$ 5. *Inorg. chem.* **2007**, *46*, 3502−3510.
(50) Mei, B.-A.; Munteshari, O.; Lau, J.; Dunn, B.; Pilon, L. Physical interpretations of Nyquist plots for EDLC electrodes and devices. *J. Phys. Chem. C* **2018**, *122*, 194−206.
(51) Ueda, T.; Ohnishi, M.; Kawamoto, T.; Guo, Si-X.; Boasc, J. F.; Bond, A. M. Voltammetric behavior of 1- and 4-$[S_2VVW_{17}O_{62}]^{5-}$ in acidified acetonitrile. *Dalton Trans.* **2015**, *44*, 11660−11668.
(52) Barthwal, S.; Singha, B.; Singh, N. B. A novel electrochemical sensor fabricated by embedding ZnO nano particles on MWCNT for morphine detection. *Mater. Today* **2018**, *5*, 9061−9066.
(53) Abraham, P.; Renjini, S.; Vijayan, P.; Nisha, V.; Sreevalsan, K.; Anithakumary, V. Review on the Progress in Electrochemical Detection of Morphine Based on Different Modified Electrodes. *J. Electrochem. Soc.* **2020**, *167*, No. 037559.
(54) Cho, E.; Perebikovsky, A.; Benice, O.; Holmberg, S.; Madou, M.; Ghazinejad, M. Rapid iodine sensing on mechanically treated carbon nanofibers. *Sensors* **2018**, *18*, 1486.
(55) Ibupoto, Z. H.; Khun, K.; Willander, M. A selective iodide ion sensor electrode based on functionalized ZnO nanotubes. *Sensors* **2013**, *13*, 1984−1997.
(56) Nosuhi, M.; Nezamzadeh-Ejhieh, A. An indirect application aspect of zeolite modified electrodes for voltammetric determination of iodate. *J. Electroanal. Chem.* **2018**, *810*, 119−128.
(57) Manivel, A.; Sivakumar, R.; Anandan, S.; Ashokkumar, M. Ultrasound-Assisted Synthesis of Hybrid Phosphomolybdate−Polybenzidine Containing Silver Nanoparticles for Electrocatalytic Detection of Chlorate, Bromate and Iodate Ions in Aqueous Solutions. *Electrocatalysis* **2012**, *3*, 22−29.
(58) Adekunle, A. S.; Arotiba, O. A.; Mamba, B. B. Electrochemical studies and sensing of iodate, periodate and sulphite ions at carbon nanotubes/Prussian blue films modified platinum electrode. *Int. J. Electrochem. Sci.* **2012**, *7*, 8503−8521.
(59) Haghighi, B.; Hamidi, H.; Gorton, L. Formation of a robust and stable film comprising ionic liquid and polyoxometalate on glassy carbon electrode modified with multiwalled carbon nanotubes: Toward sensitive and fast detection of hydrogen peroxide and iodate. *Electroch. Acta* **2010**, *55*, 4750−4757.
(60) Zou, B.-X.; Liu, X.-X.; Diamond, D.; Lau, K.-T. Electrochemical synthesis of WO_3/PANI composite for electrocatalytic reduction of iodate. *Electrochim. Acta* **2010**, *55*, 3915−3920.

https://doi.org/10.1021/acsomega.2c01287
ACS Omega 2022, 7, 43381−43389